Bulletin of the Seismological Society of America, Vol. 105, No. 3, pp. 1339–1348, June 2015, doi: 10.1785/0120140292

On the Sensitivity of Transtensional Versus Transpressional Tectonic Regimes to Remote Dynamic Triggering by Coulomb Failure

by David P. Hill

Abstract Accumulating evidence, although still strongly spatially aliased, indicates that although remote dynamic triggering of small-to-moderate ($M_w < 5$) earthquakes can occur in all tectonic settings, transtensional stress regimes with normal and subsidiary strike-slip faulting seem to be more susceptible to dynamic triggering than transpressional regimes with reverse and subsidiary strike-slip faulting. Analysis of the triggering potential of Love- and Rayleigh-wave dynamic stresses incident on normal, reverse, and strike-slip faults assuming Andersonian faulting theory and simple Coulomb failure supports this apparent difference for rapid-onset triggering susceptibility.

Introduction

Remote dynamic triggering of small-to-moderate, local earthquakes by teleseismic waves from large, distant earthquakes has been documented for a wide range of tectonic environments (Freed, 2005; Hill and Prejean, 2007, Velasco *et al.*, 2008; Parsons *et al.*, 2014; D. P. Hill and S. G. Prejean, unpublished manuscript, 2015, see Data and Resources). Spatial detection thresholds, however, remain extremely uneven because large expanses of the globe are not covered by local seismic networks, and the detection thresholds vary considerably among existing networks. Based on currently available data, it appears as though transtensional (TT) tectonic environments, including many areas of geothermal and volcanic activity, may be somewhat more susceptible to dynamic triggering than transpressional (TP) environments (Manga and Brodsky, 2005; Prejean and Hill, 2009; D. P. Hill and S. G. Prejean, unpublished manuscript, 2015, see Data and Resources). The 2002 M_w 7.9 Denali fault earthquake, for example, focused strong seismic waves across all of North America while the triggered response was limited to the extensional regimes in the western United States (Prejean *et al.*, 2004). Whether this will be borne out with more complete sampling and more uniform detection thresholds remains to be seen.

Here I explore the relative sensitivity of TT versus TP regimes (Fig. 1) to rapid-onset dynamic triggering by surface waves under Andersonian faulting theory (Sibson, 1985) and simple Coulomb failure. The background stress fields are defined by principal stresses $\sigma_1 > \sigma_2 > \sigma_3$, one of which is assumed to be the vertical, lithostatic stress (σ_v) with compression taken as positive. Effective stresses, $\sigma_i' = (\sigma_i - p)$, $i = 1, 2, 3$ are the rock matrix stresses, σ_i, reduced by the interconnected pore pressure, p. Pre-existing faults are cohesionless ($C_f \sim 0$) with friction $\mu \leq \mu_i$, in which μ_i is the internal friction of intact rock with cohesive strength, C, roughly twice the tensile strength ($C \sim 2T$). Under the Mohr circle representation of Figures 2 and 3, the Coulomb failure criteria is

$$\tau = C + \mu\sigma_n, \tag{1}$$

in which τ and σ_n are the shear and normal stress components acting on a fault plane forming an angle θ with respect to the least principal stress, σ_3. The mean stress is $\sigma_m = 1/2(\sigma_1 + \sigma_3)$ and the maximum shear stress, $\tau_m = 1/2(\sigma_1 - \sigma_3)$, occurs on a plane oriented at $\theta = 45°$ to σ_3. The stress ratio is $s = \tau_m/\sigma_m$. An optimally oriented fault at $\theta_0 = 1/2[\pi - \tan^{-1}(1/\mu)]$ corresponds to the point on the Mohr circle that is tangent to the Coulomb failure curve. All this is based on a dextral Cartesian coordinate system x, y, z with z positive upward and sign conventions as in Hill (2012a,b). The results suggest that the triggering susceptibility arrow is tipped in favor of TT regimes (see the Appendix for a list of symbols and abbreviations).

Fault and Fracture Orientations in Transtensional and Transpressional Stress Regimes

A TT regime is characterized by a combination of normal (N) and strike-slip (SS) faults with vertical extension cracks opening horizontally in the σ_3 direction. The greatest principal stress is vertical ($\sigma_1 \sim \sigma_v$) for normal faulting but rotating about σ_3 becoming subhorizontal to accommodate local SS faulting. The stress ratio associated with TT regimes is $0.5 < r < 1$, in which

$$r = (\sigma_1 - \sigma_2)/(\sigma_1 - \sigma_3), \tag{2}$$

with $r \to 0.5$ as σ_1 becomes subhorizontal (see Figs. 1 and 2).

A TP regime is characterized by a combination of reverse (R) and SS faults with horizontal cracks opening in the vertical ($\sigma_3 \sim \sigma_v$) direction. The stress ratio for TP regimes is $0.5 < r < 1$ with σ_3 becoming subhorizontal as $r \to 0.5$.

An SS regime is intermediate between the two with $\sigma_2 \sim \sigma_v$, $r \sim 0.5$, and both σ_1 and σ_3 horizontal. Extension

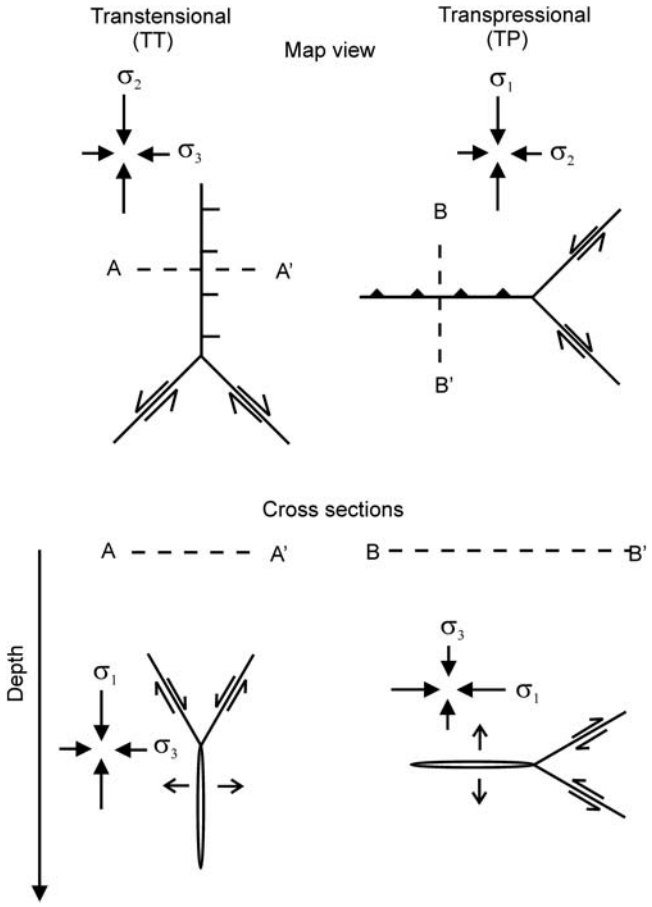

Figure 1. Schematic representation of idealized fault and fracture patterns in (left column) transtensional (TT) and (right column) transpressional (TP) stress regimes. (Top) map view and (bottom) depth sections along profiles A–A′ and B–B′, respectively.

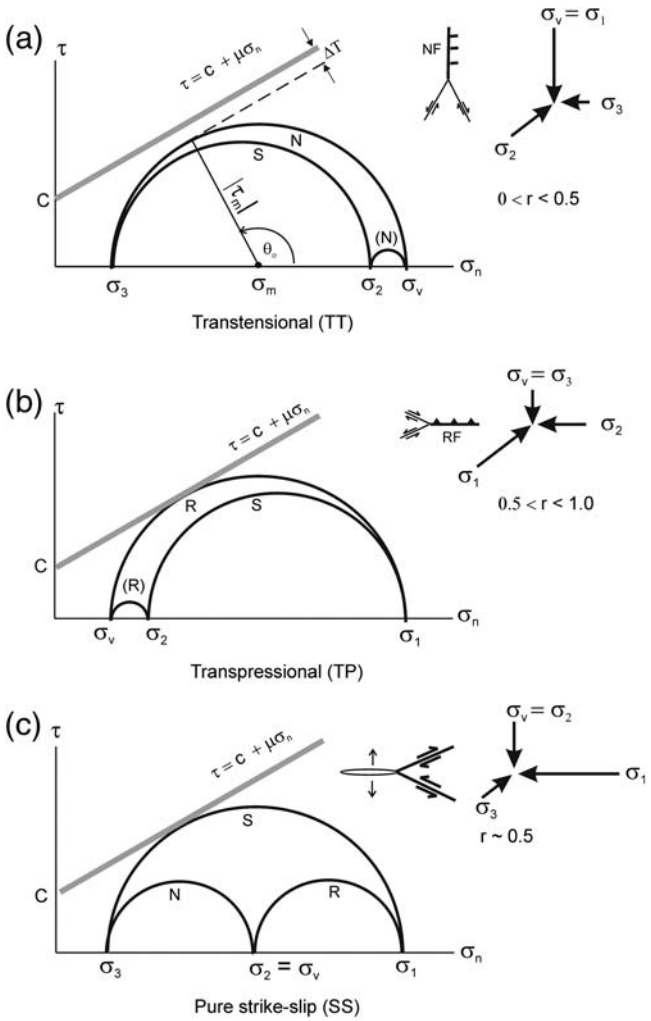

Figure 2. 3D Mohr circle diagrams characterizing the stress state in (a) TT, (b) TP, and (c) strike-slip (SS) stress regimes. The gray line indicates the Coulomb failure envelope, and $\Delta\mathbf{T} = (\Delta\sigma_n, \Delta\tau)$ is the stress increment by which the current stress state falls short of criticality (a). Arrows to the upper right of each set of circles indicate the spatial orientation of the principal stresses, $\sigma_1 > \sigma_2 > \sigma_3$ for the respective stress regimes; σ_v is the vertical principal stress. The associated fault orientations in map view are from Figure 1. N, SS, and R indicate Mohr circles associated with normal, strike-slip, and reverse faulting, respectively. In the TT regime (a), circle N is in the $\sigma_v - \sigma_3$ plane, SS is in the $\sigma_2 - \sigma_3$ plane, and (N) is in the $\sigma_v - \sigma_2$ plane. Normal faults (N) associated with the $\sigma_v - \sigma_2$ plane are far from Coulomb failure for $0 < r < 0.5$. Analogous relations hold for the TP regime (b). Reverse faults (R) associated with the $\sigma_v - \sigma_2$ plane are far from Coulomb failure for $0.5 < r < 1.0$. Note that the SS circle for the TP regime is further from Coulomb failure than in the TT regime. In the pure SS regime with $r \sim 0.5$ (c), both N and R Mohr circles are far from Coulomb failure.

cracks are vertical and perpendicular to σ_3 bisecting the planes of the conjugate SS faults (Fig. 2c).

Limiting Strength

For a common friction coefficient (e.g., $\mu \sim 0.6$) and pore pressure (e.g., hydrostatic), the shear stress required for Coulomb failure on optimally oriented reverse faults in a compressional regime will be roughly three times that required for failure on normal faults in an extensional environment at comparable depths. This occurs because (1) the vertical principal stress, σ_v (lithostatic pressure), corresponds to σ_1 for normal faults and σ_3 for reverse faults and (2) the slope of the Coulomb failure curve, $\mu = \tan(\psi)$, limits the shear (frictional) strength of faults under a stress regime with a given mean stress, $\sigma_m = 1/2(\sigma_1 + \sigma_3)$, in the $\sigma_n - \tau$ space of a Mohr circle diagram (Fig. 3).

This difference in shear strength is reflected in the ratio of the frictional energy required for an increment of slip δu on normal versus thrust faults as a function angle, θ, between the fault plane and the least principal stress, σ_3 (Fig. 4a). The frictional energy is

$$\varepsilon(\theta) = GE(\theta) = G[1 - s\cos(2\theta)/\sin(2\theta)], \qquad (3)$$

in which $G = \delta u(A\mu\sigma_m)$ and A and δu the fault area and incremental slip, respectively (Hill and Thatcher, 1992, measure θ with respect to σ_1). The normalized energy $E(\theta) = \varepsilon(\theta)/G$ is minimal for the optimal angle θ_0. For $\mu = 0.6$, $\theta_0 = 60°$, which corresponds to fault dips $\beta_N = |\theta_0| \sim 60°$ for optimally

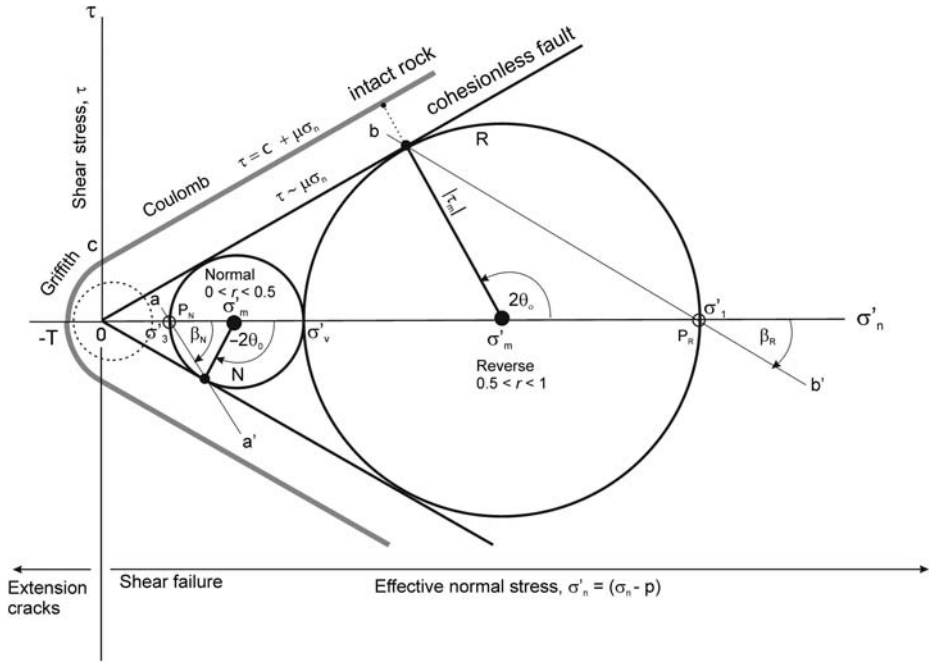

Figure 3. Mohr circle diagram illustrating relative stress levels limited by the Coulomb failure criteria for slip on pre-existing, cohesionless ($C \sim 0$), optimally oriented normal (N) and reverse (R) faults (heavy lines) at a common depth with a common pore pressure, p, and frictional strength, μ. The radius of the Mohr circles just touching the Coulomb failure envelope is the maximum amplitude of the shear stress $|\tau_m| = 1/2(\sigma_1' - \sigma_3')$ and the effective mean stress is $\sigma_m' = 1/2(\sigma_1' + \sigma_3')$. For $\mu \sim 0.6$, optimally oriented fault planes form an angle, $\theta_0 \sim 60°$ with respect to the least principal stress, σ_3. The gray band is the Coulomb–Griffith failure envelope for intact rock with internal friction taken as $\sim\mu$ and cohesive and tensile strengths C and T, respectively. Positions of the Mohr circles N and R, along the effective normal stress axis σ_n' are tied to a common vertical principal stress, $\sigma_v' = \sigma_1'$ or σ_3' for normal and reverse faults, respectively. Fault dip angles β in physical space are defined by the lines a–a′ and b–b′, which pass through the tangent points on the Mohr circles and the poles P_R and P_N for reverse and normal faults at σ_1 and σ_3, respectively (see Hill, 2012a). For pre-existing faults with cohesive strength $0 > C < 2T$, mixed mode (extensional shear) may occur if $-T > \sigma_3' < 0$ (small dashed circle). Hydrofracturing of intact rock (extension crack formation) results if the pore pressure exceeds tensile stress ($p > T$) such that $\sigma_3' \leq -T$ (see Cox, 2010).

oriented normal faults (σ_1 vertical) and $\beta_R = |\pi/2 - \theta_0| \sim 30°$ for optimally oriented thrust faults (σ_1 horizontal). The ratio of the energy required for slip on reverse with respect to normal faults both with $\mu = 0.6$ is ~3 for all angles, $0 < \theta < 90°$. This energy ratio increases monotonically as a function of friction from ~0 for $\mu = 0$ to ~6 for $\mu = 1.0$.

In the absence of optimally oriented faults, Coulomb failure may occur on pre-existing but misoriented ($\theta \neq \theta_0$), cohesionless ($C \sim 0$) faults over a range of angles for which the stress ratio

$$R = (\sigma_1'/\sigma_3') = [1 + \mu\cot(\theta)]/[1 - \mu\tan(\theta)] \qquad (4)$$

remains positive definite (Sibson, 1985; Sibson and Xie, 1998; Cox, 2010). The maximum, minimum, and lockup angles θ_L occur at the positive infinities of R at $\pi/2$ and $\theta_0/2$, as illustrated in Figure 4b (this is reversed if θ is measured with respect to σ_1 as in Hill and Thatcher, 1992). For the case of strike-perpendicular wave-incidence dip-slip faults with $\mu \sim 0.6$ considered here, normal faults become locked at shallow dips, $\beta_N \leq 30°$, and reverse faults become locked at steep dips $\beta_R \geq 60°$ (Figs. 4, 5).

For faults with finite cohesive strength or intact rock, mixed-mode, shear-extensional failure occurs when the pore pressure, p, exceeds the least principal stress, σ_3 such that $-T < \sigma_3' < 0$ (small dotted circle in Fig. 3). Hydrofracture (extensional failure) occurs when $p > |T|$ and $\sigma_3' < -T$. The range of lockup angles for misoriented faults is more restricted when the regional shear stress τ_m increases while σ_3' remains positive ($\sigma_3' > 0$). In this case, triggered slip on misoriented faults would be limited to angles $(\theta_0 - \phi_0) > \theta < (\theta_0 + \phi_0)$, in which $\phi_0 = 1/2\cos^{-1}[1 - 1/(1 + \mu\sigma_m'/C)]$ as illustrated in Figure 5 (see Nur *et al.*, 1986). For angles θ beyond this range, the stress required for slip on misoriented, pre-existing faults exceeds the shear strength of the surrounding intact rock, and new faults are formed in the intact rock with the optimal orientation θ_0. Of course, for the relatively small dynamic stresses from distant earthquakes to trigger new fractures in intact rock would require extraordinary circumstances. It is worth noting that if the effective friction within a fault zone, $\mu \to 0$ (due to mineralogy or a near-lithostatic, fault-confined pore pressure, $p_f \to \sigma_v$) slip can occur on faults with orientations over the entire quadrant $0 > \theta \leq 90°$ (Hill and Thatcher, 1992; Rice, 1992).

Surface-Wave Triggering Potential

Rayleigh waves should be more effective at triggering slip on optimally oriented normal faults than reverse faults

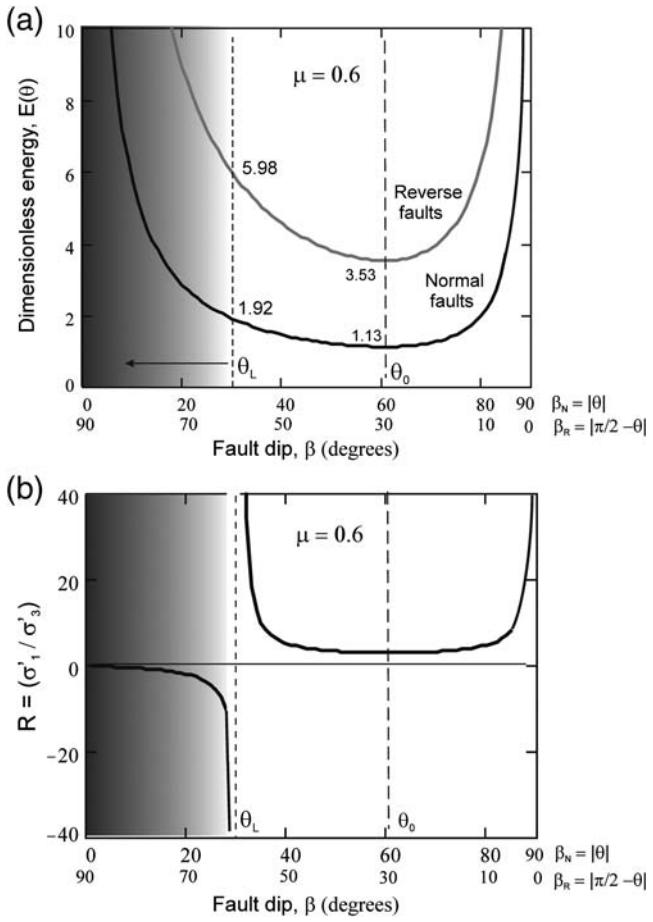

Figure 4. Minimum energy $E(\theta)$ and lockup angle for slip on normal and reverse faults with friction $\mu = 0.6$ as a function of fault inclination, θ, with respect to the least principal stress, σ_3. Note that the fault dip for reverse faults is $\beta_R = |\pi/2 - \theta|$, and for normal faults it is $\beta_N = |\theta|$. Gray shading indicates angles for fault lockup. (a) Minimum dimensionless energy, $E(\theta)$, required for slip on conjugate sets of reverse and normal faults (equation 3). The optimal angle θ_0 for fault slip coincides with the minima in the energy curves. (b) The lockup angle, $\theta_L = \theta_0/2 \sim 30°$ on cohesionless faults with $\mu \sim 0.6$ as given by the singularity in the stress ratio R (equation 4).

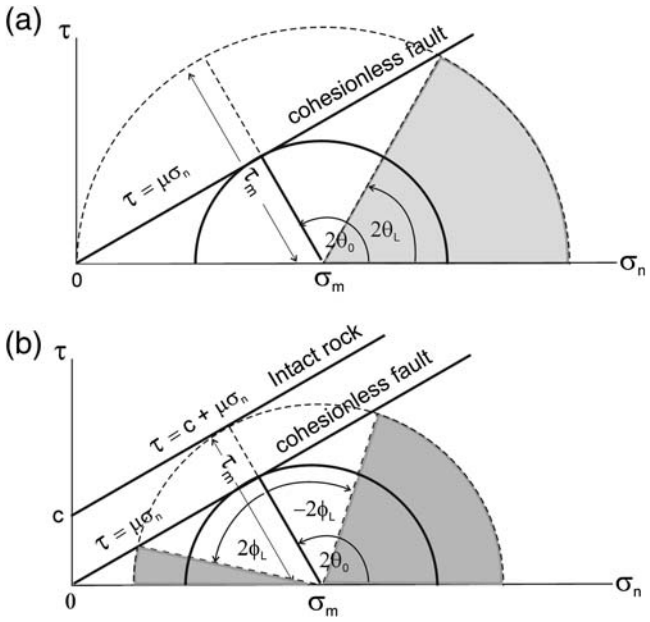

Figure 5. Mohr circle representation of lockup angles. The upper half-circles shown here apply to slip on right-dipping reverse faults. Reflecting the half-circles about the σ_n axis and reversing the signs of the angles (not shown) gives the corresponding result for slip on right-dipping normal faults (see Fig. 3). Gray wedges indicate fault-lockup inclinations. (a) Maximum misorientation (lockup) angle, θ_L for slip on nonoptimally, cohensionless reverse faults ($\theta \neq \theta_0$) corresponding to Figure 4. The large dashed circle illustrates the lockup angle, $\theta_L \sim \theta_0/2$ when the regional shear stress $|\tau_m|$ is less than the Coulomb criteria for intact rock. (b) The range of permissible slip on pre-existing, cohesionless faults is reduced if the regional shear stress $|\tau_m|$ approaches the Coulomb criteria for intact rock. In this case, slip on pre-existing cohesionless faults is restricted to $(\theta_0 + \phi_0) > \theta > (\theta_0 + \phi_0)$. An incremental increase in $|\tau_m|$ beyond the failure threshold would fracture intact rock with slip a new fault oriented at the optimal angle θ_0 (see Sibson, 1985; Nur *et al.*, 1986; Sibson and Xie, 1998).

in the upper, seismogenic crust. This is illustrated by the elliptical loci prescribed by the tip of 20 s Rayleigh-wave traction vectors acting on the positive side (right or upper side) of a dislocation surface through one wave cycle (Fig. 6). For east-dipping faults under an extensional stress field (Fig. 6a,b), the traction vector augments normal slip when fault-normal ($\delta\sigma_n$) and dip-parallel ($\delta\tau$) components are both negative by incrementally increasing the down-dip shear stress and decreasing the fault-normal stress. (Under the compression-positive stress convention, stress components are positive when acting in the negative coordinate directions.) When both components are positive, $\delta\tau$ acts counter to the much larger ambient down-dip shear stress while $\delta\sigma_n$ acts to increase the fault-normal stress thus inhibiting reverse slip. The Rayleigh-wave triggering potential on normal faults decreases with increasing depth as the aspect ratio of the stress ellipse decreases and its semimajor axis rotates counter clockwise approaching the $\delta\sigma_n$ axis (Fig. 6b).

Under a compressional stress field (Fig. 6c,d), the traction vector opposes reverse slip when both components are negative. When both components are positive, $\delta\tau$ acts to augment reverse slip while $\delta\sigma_n$ increases inhibiting reverse slip. The influence of $\delta\sigma_n$ increases with increasing depth as the aspect ratio of stress orbit increases and its semimajor axis rotates counterclockwise (Fig. 6d). For Rayleigh wave propagating to the right (east) as illustrated in Figure 6a, the traction vector rotates counterclockwise. Rayleigh-wave propagation to the west results in a clockwise rotation with the orientation of the stress orbits unchanged. For faults dipping to the left (west), the stress orbits are reflected about the vertical axis with respect to those in Figure 6 (see figs. 7 and 13 in Hill, 2012a). Major axes of stress orbits acting on extension cracks in Figure 6 are subparallel with the least principal stress, σ_3. Orbits for vertical cracks in an extensional stress field have much greater amplitudes than those on horizontal cracks in a compressional stress field.

Figure 7 provides an alternate perspective on relative susceptibility of normal versus reverse faults to triggering by

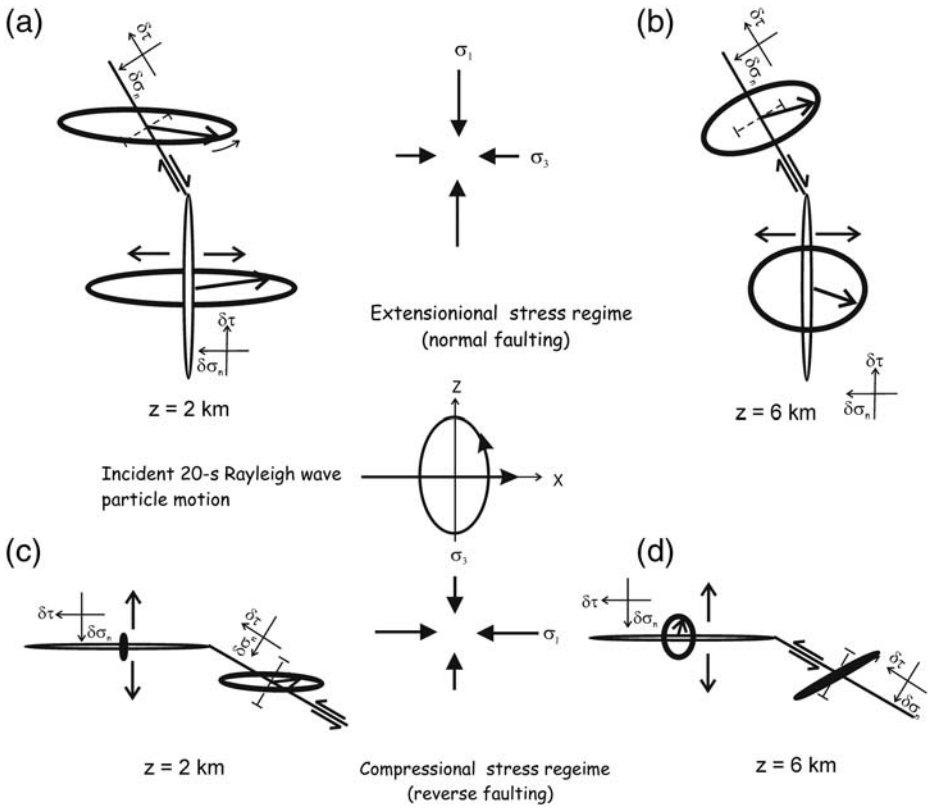

Figure 6. Rayleigh-wave stress orbits (heavy ellipses) in physical cross-section (x-z) space for 20 s waves with normal incidence ($\gamma = 90°$) on optimally oriented, east-dipping faults and extension cracks in an extensional stress regime at depths of 2 and 6 km (upper) and reverse faults in a compressional stress regime at comparable depths (lower). Orientations and signs of the dip-parallel shear ($\delta\tau$) and fault-normal ($\delta\sigma_n$) components indicated by the small coordinates in $\delta\tau - \delta\sigma_n$ space associated with each fault-fracture surface consistent with a compression-positive convention. The orbits trace the tips of the traction vectors (heavy arrows) acting on the hanging-wall fault/fracture surface. Small curved arrow in (a) indicates the counter-clockwise rotation of the traction vectors through one wave cycle of a westward propagating wave.

Rayleigh-wave dynamic stresses as a function of depth through the orientations of the stress orbits in $\delta\sigma_n - \delta\tau$ space and their proximity to the Coulomb failure envelope in a Mohr circle diagram (see Hill, 2012a).

The above examples are based on Rayleigh waves in a half-space with fault-normal incidence on inclined faults. More generally, the triggering potential of surface waves on critically oriented faults depends strongly on incidence angle and depth. This is best illustrated by plotting triggering potential as a function of incidence angle, γ, for Love and Rayleigh waves with the same period and displacement amplitudes as in Figure 8. The relative triggering potential $P(\gamma)$ is the projection of the traction vector $\delta\mathbf{T}$ touching the point on the stress orbit that is tangent to the Coulomb failure envelope (or $\delta\mathbf{T} \cdot \mathbf{n}$, where $\mathbf{n}$ is the unit normal vector to the failure envelope) normalized by the maximum magnitude of $|\delta\mathbf{T}|_{\max} = \delta T_m$ through one complete cycle, or

$$P(\gamma) = |\delta\mathbf{T} \cdot \mathbf{n}/\delta T_m| = |(\delta T/\delta T_m)\sin[\psi - a(\gamma)]| \quad (5)$$

as illustrated in Figure 8a. In comparing Love- and Rayleigh-wave potentials in the same plot, $\delta\tau_m$ is taken as that for the larger of the two stress ellipses. $P(\gamma)$ is thus proportional to the stress increment $\Delta\mathbf{T}$ of Figure 2a. $P(\gamma)$ is a relative potential, however, in that absolute value of the background shear stress, τ_m, and the proximity of the Mohr circle to the Coulomb failure envelope is seldom known. In this sense, $P(\gamma)$ is a dynamic analog to the static Coulomb failure function (Harris, 1998).

Love- and Rayleigh-wave triggering potentials for incidence on optimally oriented normal faults at a 6 km depth exceed those for optimally oriented reverse faults for all incidence angles except for near strike-parallel incidence $\gamma \sim 0°$ (Fig. 8c). There, the Rayleigh-wave potential, although small ($P(\gamma) < 0.1$), is slightly greater for reverse faults than for normal faults. The Love-wave triggering potential for normal faults, Ln, with peaks at $\gamma = \pm 45°$ exceeds the Rayleigh-wave potential for most incidence angles except in the vicinity of its nulls at $\gamma = \pm 90°$ and 0°. The peak amplitude of the Love-wave potential for reverse faults, Lr, is slightly smaller than that for Rayleigh waves on normal faults, Rn, and exceeds Rn for incidence angles $\gamma < |45°|$. Thus it seems that Love-wave triggering potentials should be comparable in TP and TT regimes depending on the incidence angle, γ, and the stress increment, $\Delta\mathbf{T}$, short of Coulomb failure in each regime.

For incidence on vertical, SS faults, Love-wave potentials dominate with peak potentials of $P(\gamma) = 1.0$ compared with peak Rayleigh-wave potentials of $P(\gamma) \sim 0.4$ (Fig. 8d). Ray-

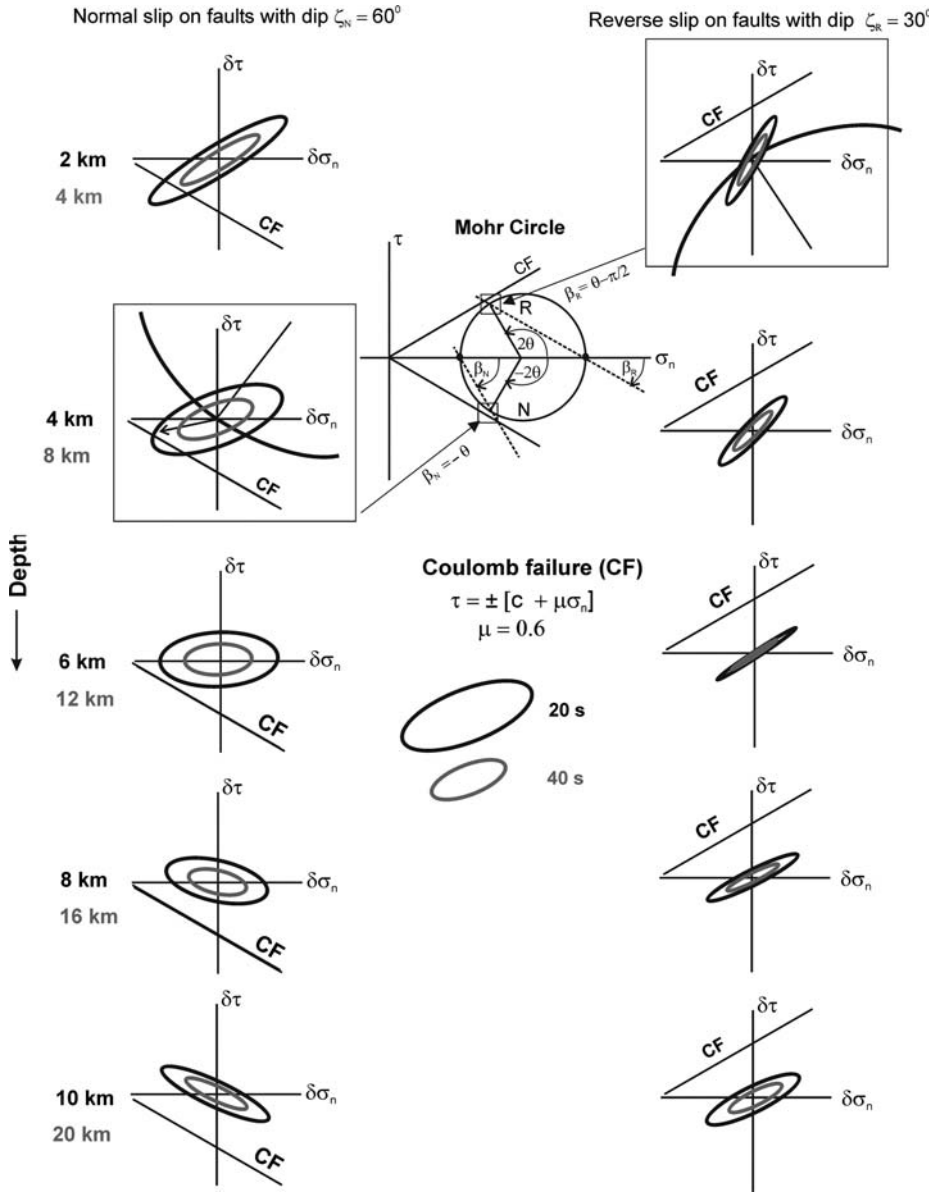

Figure 7. Variations of dynamic stress orbits in Mohr circle $\delta\tau - \delta\sigma_n$ space for 20 and 40 s Rayleigh waves with fault-normal incidence on optimally oriented normal faults (left column with dip, $\beta = |\theta| \approx 60°$) and reverse faults (right column with dip, $\beta = |\pi/2 - \theta_0| \approx 30°$) at depths from 2 to 20 km. Black and gray orbits are for wave periods of 20 and 40 s, respectively, both with the same displacement amplitude at the surface. The orbits trace the tip of the perturbing traction vector acting on a fault through one complete Rayleigh-wave cycle. The centers (origin) of the orbits coincide with the point on the Mohr circle corresponding to optimally oriented faults. The line CF is the Coulomb failure envelope in the upper half-circle for reverse faults and lower half-circle for normal faults (see inset in center column). The calculations are for Rayleigh waves in a half-space with wavelength the scale factor. Thus, the orbit for 40 s waves at 4 km is similar to that for 20 s waves at 2 km but with half the amplitude (stress varies inversely with period for waves of the same displacement amplitude).

leigh- and Love-wave peaks and troughs are anticorrelated such that Rayleigh waves have a greater triggering potential in the vicinity of nulls in the Love-wave potential. The positions of the peaks and troughs vary with incidence angle γ depending on the sense of strike-parallel slip (right versus left lateral) and the coefficient of friction. For frictionless faults, the potential curves are symmetric about $\gamma = 0°$ (fig. 10 in D. P. Hill and S. G. Prejean, unpublished manuscript, 2015, see Data and Resources). For finite friction, $\mu > 0$, the curves are shifted to the right or left for incidence on faults with right-lateral or left-lateral slip, respectively. The amount of shift varies with μ. The example in Figure 8d is for wave incidence at a depth of 6 km with on faults of $\mu = 0.6$.

Based on Figure 8d, it would seem that surface-wave triggering potential for triggering slip on vertical, SS faults is the same for TT and TP regimes. The 3D Mohr circles in Figure 2, however, suggest that the susceptibility arrow tips in favor of TT regimes. In particular, the TP SS Mohr circle in the $\sigma_1 - \sigma_2$ plane with $r < 0.5$ (Fig. 2b) is further from the Coulomb failure curve than the TT SS circle in the $\sigma_2 - \sigma_3$ plane with $r > 0.5$ (Fig. 2a).

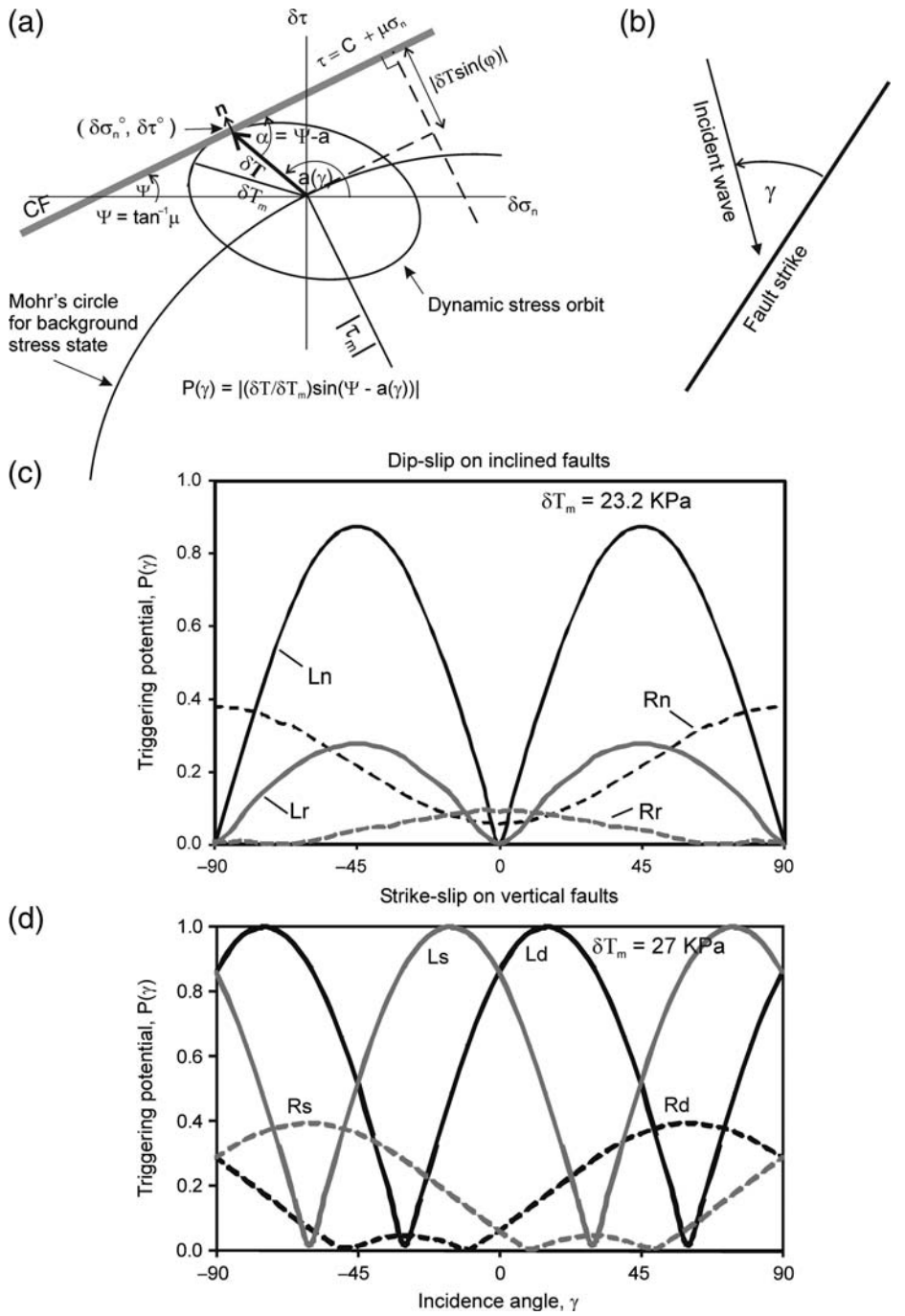

Figure 8. Surface-wave triggering potentials $P(\gamma)$ as a function of incidence angle, γ, on faults at a depth of 5 km with $\mu = 0.6$. (a) Schematic definition of $P(\gamma)$. δT is the amplitude of the traction vector touching the point on the stress ellipse tangent to the Coulomb failure envelope (gray line). δT_{m} is maximum amplitude of the traction vector (the half-length of the semimajor axis). (b) Convention for the wave incidence angle, γ, with respect to the fault strike. (c) Potential $P(\gamma)$ for triggering dip slip by waves incident on inclined faults. *Ln* and *Rn* are potentials for Love and Rayleigh waves incident on optimally oriented normal faults ($\beta_{\mathrm{N}} \sim 60°$). *Lr* and *Rr* are potentials for optimally oriented reverse faults ($\beta_{\mathrm{R}} \sim 30°$). Love-wave and Rayleigh-wave potentials indicated by solid and dashed lines, respectively. (d) Potential $P(\gamma)$ for triggering strike-parallel slip by waves incident on vertical faults. Gray curves are for sinistral slip (*Ls*, *Rs*) and black curves for dextral slip (*Ld*, *Rd*).

Discussion

These results are based on plane-wave propagation in simple, homogeneous, crustal models (the Rayleigh-wave model is a half-space and the Love-wave model is a 30 km thick layer over a half-space) and the assumption that pore pressures are the same everywhere (e.g., hydrostatic). Of course the expectations outlined above are first-order approximations to the real Earth with its 3D structural and stress-field

heterogeneities. Wave propagation through heterogeneous and/or anisotropic velocity structures, for example, often results in multipathing and coupling between Love and Rayleigh waves (Hill *et al.*, 2013; Agnew and Wyatt, 2014).

Crustal fluids have an important role in triggering potential as they modulate frictional strength and effective stress through interconnected pore pressure, p, or elevated, fault-confined pore pressure, p_f. The assumption that all faults have approximately the same frictional strength ($\mu \sim 0.6$) may be approximately true for areas with dominantly hydrostatic pore pressures and widely distributed faulting such as the TT Basin and Range province or the midcontinental TP regime. Systematic variations in pore pressures between stress provinces (or subregions thereof), however, will produce corresponding variations in the effective vertical stress, σ_v, thus uncoupling the relation between Mohr circles illustrated in Figure 3. If, for example, the pore pressure in a TP regime exceeded that in a TT regime by $\Delta P = (\sigma_v^{(R)} - \sigma_3^{(N)})$, the respective Mohr circles would coincide, and faults in the two regimes would have comparable shear strengths. In addition, cyclical dilation of vertical extension cracks by Rayleigh waves propagating in a TT regime (Fig. 6) will act to augment the upward transport of high-pressure fluids at depth thereby weakening faults at shallower depths. This hydraulic pumping action is much less efficient for horizontal cracks in a compressional or TP stress field.

Mature, through-going faults transecting a tectonic stress regime tend to be weaker than surrounding faults in a given stress regime. The San Andreas fault through central California, for example, is demonstrably weaker than the stronger reverse and SS faults in the surrounding TP stress regime (Townend and Zoback, 2004). Yet the San Andreas fault through the Parkfield section with its high seismicity rates in the upper, seismogenic crust (depths < 15 km) has been notably insensitive to dynamic triggering (Spudich *et al.*, 1995). This stands in contrast to the deeper, transitional section of the fault extending through the lower crust (depths between ~15 to 30 km), which responds frequently with tectonic tremor triggered by both body and surface waves from strong teleseismic earthquakes (Peng *et al.*, 2008; Hill *et al.*, 2013). Evidence suggests that this contrast may be due to near-lithostatic, fault-confined pore pressures in the tremorgenic section of the fault zone (e.g., D. P. Hill and S. G. Prejean, unpublished manuscript, 2015, see Data and Resources).

The surface-wave triggering potentials in Figure 8c,d are for Love and Rayleigh waves with the same period (20 s) and displacement amplitude at the surface (0.01 m). In general, the amplitude of waves of a given period recorded at a specific site differs depending on the source radiation pattern and directivity and epicentral distance. For recorded Love and Rayleigh waves of the same period at a given site, the relative potentials in Figure 8 can be scaled by the ratio of the observed amplitudes. The potentials need to be computed separately, however, for different periods at various depths.

Love-wave triggering potentials generally exceed Rayleigh-wave potentials over a wide range of incidence angles (Fig. 8) with the exception of reverse faults in TP regimes (Fig. 8c). There, the triggering potentials are comparable depending on incidence angles. Love-wave triggering potentials on vertical, SS faults dominate those for Rayleigh waves (Fig. 8d) over a broad range of incidence angles. This certainly applies to simple SS regimes with $r \sim 0.5$ (Fig. 2c) and to TT regimes with $0 \leq r < 0.5$ (Fig. 2a). Critically oriented SS faults in TP regimes, however, should be less susceptible to Love-wave triggering unless the stress ratio $1 \sim r > 0.75$ and the SS Mohr circle approaches the size of the reverse (R) circle (Fig. 2b).

Finally, stable cratons, many of which are TP, generally have lower stressing rates than most TT regimes (e.g., the Basin and Range province versus the North American craton east of the Rocky Mountains). Thus, for a given stress drop (due, say, to local earthquake or a triggered earthquake sequence), the stress state in tectonically active TT regimes will return to a critical state more frequently than in a stable TP regime. Accordingly one might expect more areas within a TT regime to be in a near-critical state at any given time than in a TP regime. This is consistent with a higher seismicity rate in the TT regime of the western United States compared with the stable TP regime of the central and eastern parts of the country. It does not apply to tectonically active compressive and TP regimes associated with subduction zones and mountain building.

Conclusions

This analysis of dynamic triggering potential for surface waves incident on faults in the upper, brittle crust assuming Andersonian-faulting theory and simple Coulomb failure suggests that TT tectonic regimes should be more susceptible to remote dynamic triggering than TP regimes. Love-wave triggering potentials generally exceed those for Rayleigh waves over a broad range of incidence angles in TT and SS regimes. For incidence angles, $\gamma < |45°|$, however, Love-wave triggering potentials on optimally oriented reverse faults exceed those for Rayleigh-wave potentials on optimally oriented normal faults (Fig. 8c), suggesting that Love waves should have comparable triggering capability in both TT and TP regimes. Understanding why we do not see more evidence for Love-wave triggering in stable TP regimes may shed light on variations in proximity of the stress state ($\Delta\mathbf{T}$ in Fig. 2a) between regimes.

The results apply to rapid-onset triggering on faults under a near-critical stress field. In this case, frictional failure (triggering) occurs as the dynamic traction vectors acting on a fault surface first boosts the local tectonic stress over the pressure-sensitive Coulomb failure threshold. Rapid-onset triggering most commonly involves small-to-moderate earthquakes ($M_w \leq 5$) with source dimensions as a fraction of the surface-wave wavelengths such that the perturbing stress has the same phase over much of the earthquake rupture surface.

Short delays (seconds to tens of minutes) in a triggered response may result from the dilatational component of Rayleigh waves acting on vertical cracks (Fig. 6a,b) to induce diffusion of elevated pore pressures to shallower depths through hydraulic pumping. More elaborate pressure-sensitive friction

laws such as rate-state friction also admit the possibility of small delays in triggering depending on the parameters in the evolution law for the state variable (Dieterich, 2007).

The direct action of dynamic stresses on fault planes considered in this analysis will not necessarily apply to onset of remotely triggered seismicity delayed by hours to days or more with respect to the passing dynamic stresses from a distant earthquake. If a causal link can be established in such cases, the putative triggered seismicity is likely a secondary response to a local aseismic deformation source initially triggered by the passing dynamic stresses such as fault creep or a volume increase associated with geothermal system or magma body (D. P. Hill and S. G. Prejean, unpublished manuscript, 2015, see Data and Resources). Nor will it likely apply to the rare instances of large ($M_w > 5$), potentially damaging triggered earthquakes with source dimensions greater than 10 s of kilometers and delays of days to weeks (Parsons *et al.*, 2012, 2014; Pollitz *et al.*, 2012).

As instrumental capabilities expand for a more uniform detection of remote dynamic triggering around the globe, the ability to calculate *in situ* dynamic stress perturbations propagating as teleseismic waves from large, distant earthquakes coupled with an appreciation of the associated triggering potential in diverse tectonic regimes promises to provide new insight on the state of stress in the crust and variations in its proximity to criticality.

Data and Resources

Computations were made using Mathcad 15. Unpublished manuscript by D. P. Hill and S. G. Prejean (2015). *Dynamic triggering*, in *Earthquake Seismology*, H. Kanamori (Editor), *Treatise on Geophysics*, second Edition, G. Shubert (Editor-in-Chief), Vol. 4, chapt. 78, Elsevier, Amsterdam, the Netherlands. All other resources are taken from sources cited in the text and given in the reference section of this paper.

Acknowledgments

I much appreciate the thorough and constructive reviews of the original manuscript by Tom Parsons and two anonymous reviewers. A careful reading by reviewer number 1 identified a number of notation inconsistencies that spurred construction of the Appendix and a more systematic use of symbols. I am grateful to my colleague Stephanie Prejean for our ongoing discussions and collaboration on dynamic triggering issues.

References

Agnew, D. C., and F. K. Wyatt (2014). Dynamic strains at regional and teleseismic distances, *Bull. Seismol. Soc. Am.* **104,** 1846–1859.

Cox, S. F. (2010). The application of failure mode diagrams for exploring the roles of fluid pressure and stress states in controlling styles of fracture-controlled permeability enhancement in faults and shear zones, *Geofluids* **10,** doi: 10.1111/j.1468-8123.2010.00281.x.

Dieterich, J. H. (2007). Application of rate- and state-dependent friction to models of fault slip and earthquake occurrence, in *Earthquake Seismology*, H. Kanamori (Editor), in Treaties on Geophysics, G. Schubert (Editor-in-Chief), Vol. 4, Elsevier, Amsterdam, the Netherlands, 107–129.

Freed, A. M. (2005). Earthquake triggering by static, dynamic, and postseismic stress transfer, *Annu. Rev. Earth Planet. Sci.* **33,** 335–367.

Harris, R. A. (1998). Introduction to a special section: Stress triggers, stress shadows, and implications for seismic hazards, *J. Geophys. Res.* **103,** 24,347–24,358.

Hill, D. P. (2012a). Dynamic stresses, Coulomb failure, and remote triggering —Corrected, *Bull. Seismol. Soc. Am.* **102,** doi: 10.1785/0120120085.

Hill, D. P. (2012b). Surface-wave potential for triggering tectonic (nonvolcanic) tremor—Corrected, *Bull. Seismol. Soc. Am.* **102,** doi: 10.1785/0120120086.

Hill, D. P., and S. G. Prejean (2007). Dynamic triggering, in *Earthquake Seismology*, H. Kanamori (Editor), Treatise on Geophysics, G. Shubert (Editor-in-Chief), Vol. 4, Elsevier, Amsterdam, The Netherlands, 257–291.

Hill, D. P., and W. Thatcher (1992). An energy constraint for frictional slip on misoriented faults, *Bull. Seismol. Soc. Am.* **82,** 883–897.

Hill, D. P., Z. Peng, D. R. Shelly, and C. Aiken (2013). *S*-wave triggering of tremor beneath the Parkfield, California, section of the San Andreas fault by the 2011 Tohoku, Japan, earthquake: Observations and theory, *Bull. Seismol. Soc. Am.* **103,** 1541–1550, doi: 10.1785/0120120114.

Manga, M., and E. Brodsky (2005). Seismic triggering of eruptions in the far field: Volcanoes and geysers, *Annu. Rev. Earth Planet. Sci.* **34,** 263–291.

Nur, A., H. Ron, and O. Scotti (1986). Fault mechanics and the kinematics of block rotations, *Geology* **14,** 746–749.

Parsons, T., J. O. Kaven, A. A. Velasco, and H. Gonzales-Huizar (2012). Unraveling the apparent magnitude threshold of remote earthquake triggering using full wavefield surface wave simulation, *Geochem. Geophys. Geosyst.* **13,** doi: 10.1029/2012GC004164.

Parsons, T., M. Segou, and W. Marzocchi (2014). The global aftershock zone, *Tectonophysics* **618,** 1–34.

Peng, Z., J. E. Vidale, K. C. Creager, J. L. Rubinstein, J. Gomberg, and P. Bodin (2008). Strong tremor near Parkfield, CA, excited by the 2002 Denali fault earthquake, *Geophys. Res. Lett.* **35,** L23305, doi: 10.1029/2008GL036080.

Pollitz, F. F., R. S. Stein, V. Sevilgen, and R. Bürgmann (2012). The 11 April east Indian Ocean earthquake triggered large aftershocks worldwide, *Nature* **408,** 250–253.

Prejean, S. G., and D. P. Hill (2009). Earthquakes, dynamic triggering of, in *Complexity in Earthquakes, Tsunamis, and Volcanoes, and Forecast*, R. Meyers (Editor), Springer, Berlin, Germany, 2600–2621.

Prejean, S. G., D. P. Hill, E. E. Brodsky, E. E. Hough, M. J. S. Johnston, S. D. Malone, D. H. Oppenheimer, A. M. Pitt, and K. B. Richards-Dinger (2004). Remotely triggered seismicity on the United States west coast following the M_w 7.9 Denali fault earthquake, *Bull. Seismol. Soc. Am.* **94,** S348–S359.

Rice, J. R. (1992). Fault stress states, pore pressure distributions, and the weakness of the San Andreas fault, in *Fault Mechanics and Transport Properties of Rocks*, B. Evans and T.-F. Wong (Editors), Chapter 20, Academic Press, San Francisco, California, 476–503.

Sibson, R. H. (1985). A note on fault reactivation, *J. Struct. Geol.* **7,** 751–754.

Sibson, R. H., and G. Xie (1998). Dip range for intracontinental reverse fault ruptures: Truth not stranger than friction? *Bull. Seismol. Soc. Am.* **88,** 1014–1022.

Spudich, P., L. K. Steck, M. Hellweg, J. B. Fletcher, and L. M. Baker (1995). Transient stresses at Parkfield, California, produced by the M 7.4 Landers earthquake of June 28, 1992: Observations from the UPSAR dense seismograph array, *J. Geophys. Res.* **100,** 675–690.

Townend, J., and M. D. Zoback (2004). Regional tectonic stress near the San Andreas fault in central and southern California, *Geophys. Res. Lett.* **31,** L15S11, doi: 10.1029/2003GL018918.

Velasco, A. A., S. Hernandez, T. Parsons, and K. Pankow (2008). Global ubiquity of dynamic earthquake triggering, *Nature Geosci.* **1,** 375–379.

Appendix

Table A1 lists the symbols and abbreviations used in this article.

Table A1
Symbols and Abbreviations

A	Area of incremental slip, δu, on a fault
N, SS, R	Normal, strike-slip, and reverse faults, respectively
TT, TP	Abbreviations for transtensional and transpressional, respectively
CF	Coulomb failure threshold (Fig. 7)
C	Cohesive strength
T	Tensile strength
$P(\gamma)$	Relative triggering potential as a function of incidence angle
$\mathbf{n}$	Unit-normal vector to the Coulomb failure envelope (Fig. 8a)
μ	Coefficient of friction
$\sigma_1 > \sigma_2 > \sigma_3$	Principal stresses, compression positive
$\sigma_{\mathrm{i}}^{'} = (\sigma_{\mathrm{i}} p), i = 1, 2, 3$	Effective stress, p is interconnected pore pressure
$\sigma_{\mathrm{i}}^{(N)}, \sigma_{\mathrm{i}}^{(R)}$	Stress components on normal and reverse faults
$\sigma_{\mathrm{m}} = 1/2(\sigma_1 + \sigma_3)$	Mean stress
σ_{n}	Fault-normal stress
σ_{v}	Vertical principal stress
τ	Fault-parallel shear stress
$\tau_{\mathrm{m}} = 1/2(\sigma_1 - \sigma_3)$	Maximum shear stress (occurs on faults at $\theta = 45°$ to σ_3)
$\lvert\tau_{\mathrm{m}}\rvert$	Radius of a Mohr circle (Fig. 3)
$\delta\sigma_{\mathrm{n}}(t)$, $\delta\tau(t)$	Fault-normal and fault-parallel dynamic stress components
$\delta\mathbf{T}(t) = [\delta\sigma_{\mathrm{n}}(t), \delta\tau(t)]$	Dynamic traction vector acting on a fault plane
δT_{m}	Maximum amplitude of $\delta\mathbf{T}(t)$ through one complete wave cycle
δu	Slip increment on a fault
ΔT	Stress difference between CF threshold and $\tau(\theta_0)$ (Fig. 2a)
p	Interconnected pore pressure
p_{f}	Fault-confined pore pressure
$R = \sigma_1^{'}/\sigma_3^{'}$	Ratio of greatest to least principal stress
$r = (\sigma_1 - \sigma_2)/(\sigma_1 + \sigma_3)$	Ratio of intermediate- to greatest-principal stress differences
$s = \tau_{\mathrm{m}}/\sigma_{\mathrm{m}}$	Ratio of maximum shear stress to mean stress
θ	Angle between greatest principal stress, σ_1, and a fault plane
θ_0	Optimum angle for fault slip in a given stress field
θ_{L}	Lockup angle (Figs. 4, 5)
$\theta_0 \pm \phi_0$	Maximum and minimum lockup angles with respect to θ_0 (Fig. 5)
γ	Incidence angle of seismic wave on fault plane
ψ	Angle between the Coulomb failure envelope and σ_{n} (Fig. 8a)
$a(\gamma)$	Angle of $\delta\mathbf{T}$ with respect to σ_1 (Fig. 8a)
$\alpha(\gamma)$	$\psi - a(\gamma)$ (Fig. 8a)
β_{N}, β_{R}	Dip angles for normal and reverse faults
$\mathcal{E}(\theta)$	Frictional energy for an increment of slip, δu, on a fault of area, A
$E(\theta) = \mathcal{E}(\theta)/G$	Dimensionless energy = $[1 - \rho\cos(2\theta)]/\sin(2\theta)$
$G = \delta u A \mu \sigma_{\mathrm{m}}$	Energy normalization factor

U.S. Geological Survey
Volcano Science Center
MS 910
345 Middlefield Road
Menlo Park, California 94025
hill@usgs.gov

Manuscript received 30 September 2014;
Published Online 28 April 2015